Two-level system hyperpolarization using a quantum Szilard engine

Martin Spiecker [1,2] ✉, Patrick Paluch [1,2], Nicolas Gosling [2], Niv Drucker[3],
Shlomi Matityahu[4], Daria Gusenkova[1,2], Simon Günzler [1,2], Dennis Rieger [1,2],
Ivan Takmakov[1,2], Francesco Valenti [2], Patrick Winkel [1,2], Richard Gebauer[5],
Oliver Sander[5], Gianluigi Catelani [6], Alexander Shnirman[2,4],
Alexey V. Ustinov[1,2], Wolfgang Wernsdorfer [1,2], Yonatan Cohen[3]
& Ioan M. Pop [1,2]✉

The innate complexity of solid-state physics exposes superconducting quantum circuits to interactions with uncontrolled degrees of freedom degrading their coherence. By implementing a quantum Szilard engine with an active feedback control loop, we show that a superconducting fluxonium qubit is coupled to a two-level system (TLS) environment of unknown origin, with a relatively long intrinsic energy relaxation time exceeding 50 ms. The TLSs can be cooled down, resulting in a four times lower qubit population, or they can be heated to manifest themselves as a negative-temperature environment corresponding to a qubit population of ~80%. We show that the TLSs and qubit are the dominant loss mechanism for each other and that qubit relaxation is independent of the TLS populations. Understanding and mitigating TLS environments is, therefore, not only crucial to improve the qubit lifetimes but also to avoid non-Markovian qubit dynamics.

Although tremendous progress has been made to improve the coherence of superconducting qubits, they still have to cope with various loss and decoherence mechanisms, certainly to the chagrin of quantum computing scientists but also to the joy of mesoscopic physicists. The relentless interactions between superconducting hardware and its environment motivate the development of quantum error correction using stabilizer codes on one hand[1–4] and deepen our understanding of mesoscopic processes on the other hand[5–15]. In the past, numerous strategies have been conceived to study and mitigate decoherence from various sources, from defects in dielectrics to non-thermal excitations[16]. A major source can be attributed to the wide class of two-level system (TLS) in the qubit environment. Weakly coupled TLSs may be investigated by saturation pulses[17,18], whereas strongly coupled TLSs may even be coherently operated via the superconducting qubit[19,20]. Moreover, it has been shown that a sequence of repeated π pulses can change the environment of the superconducting qubit, which was interpreted as the diffusion of superconducting quasiparticles away from the qubit junctions[9].

Here we implement a quantum Szilard engine[21–24] that manipulates the environment of a superconducting qubit. Our Szilard engine executes a hyperpolarization protocol similar to experiments using spin qubits[25] or defect centres[26], and is readily applicable in state-of-the-art quantum processors[27–29]. The hyperpolarized environment reveals that the qubit is weakly coupled to a TLS environment of unknown origin, which relaxes over tens of milliseconds. Conversely, this previously hidden environment can now be identified as the dominant loss mechanism of our qubit, and we dread that similarly acting environments are ubiquitous in superconducting hardware. The quantum Szilard engine consists of a granular aluminium fluxonium qubit[30] that can be actively prepared in one of its eigenstates |g⟩ or |e⟩. The fluxonium and its complex environment are depicted in Fig. 1a. The Szilard engine implements a dynamical polarization protocol on the TLSs (Fig. 1b,c). In contrast to
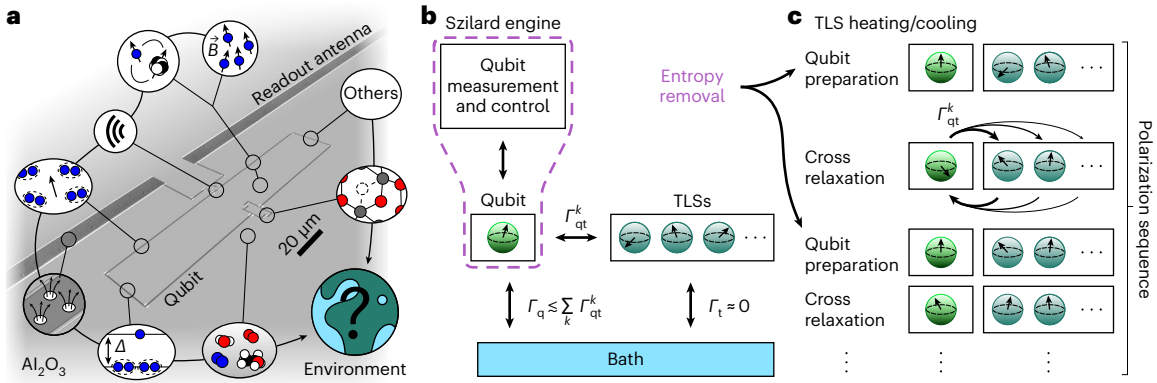
Fig. 1 | Superconducting qubit, its environment and working principle of the Szilard engine. a, Schematic of the fluxonium qubit inductively coupled to its readout antenna. The rich environment typical for superconducting circuits is shown and includes (counterclockwise) the following: free electronic spins that may be Zeeman split by an external magnetic field[45,46] or via a hyperfine interaction[47], radiation loss into the readout and qubit drive ports[48] or into spurious modes including phonons[49], Shiba spins[42], trapped vortices[50,51], quasiparticles, absorbed molecules on the surface[52] and dielectric TLSs[53]. The fluxonium is implemented with granular aluminium and a superconducting quantum interference device junction[30,31]. **b**, Qubit environment can be modelled as a collection of polarizable TLSs and a global bath responsible for the so-called intrinsic loss of both qubit (Γ_q) and TLSs (Γ_t). As shown later, in our case, the TLSs act as a heat reservoir, because they provide the main relaxation channel for the qubit ($\Gamma_q \lesssim \sum_k \Gamma_{qt}^k$) and being approximately lossless ($\Gamma_t \approx 0$). **c**, Schematic of the qubit and TLS populations during the polarization sequence. Each cycle of the Szilard engine consists of a qubit preparation followed by the cross relaxation between the qubit and TLSs. After each cycle, the polarization of the TLSs increases.

nuclear hyperpolarization, here the qubit and TLSs operate in the same frequency domain, requiring active or autonomous feedback schemes.

The experimental workflow (Fig. 2a) starts with a polarization sequence where we stabilize the qubit in either $|g\rangle$ or $|e\rangle$, thereby cooling or heating the reservoir, respectively. After polarizing the reservoir, the qubit is initialized in $|g\rangle$ or $|e\rangle$ and the combined qubit and reservoir system relaxes to its steady state. As an example (Fig. 2b), we show the qubit population before and after the first preparation in a sequence polarizing to $|e\rangle$. The amount of heat in the reservoir, that is, the degree of TLS polarization, varies with the operation time of the Szilard engine, given by the number of qubit preparations N. Correspondingly, in Fig. 2c, we show the measured decrease in qubit transition rates $\Gamma_{\uparrow,\downarrow}$ during stabilization in $|g\rangle$ or $|e\rangle$, respectively. The different polarization and initialization scenarios are measured interleaved with $M = 2,500$ repetitions for each scenario, which sets the uncertainties visible as noise in the measured curves.

The relaxation of the reservoir cannot be directly observed and has to be inferred from the qubit dynamics. Although the common approach is to measure the free decay of the qubit (Supplementary Section A), here we exploit the fact that the qubit readout is more than 96% quantum non-demolishing (Supplementary Section B and ref. 31) and we perform repeated single-shot readouts, resulting in stroboscopic quantum-jump traces (Fig. 2d). The main benefit of this method is the direct determination of transition rates $\Gamma_{\uparrow,\downarrow}$ between the ground and excited state, which allows us to discriminate between changes in the energy relaxation rate and changes in the equilibrium population of the qubit. In Fig. 3, we show the measured qubit relaxation curves for several polarization and initialization scenarios. Note that for long enough polarization times to the excited state ($N \geq 10^3$), the qubit reaches population inversion (Fig. 3c, bottom), which hints at a population inversion of the reservoir. This effect is also confirmed by the inversion of the transition rates $\Gamma_\uparrow > \Gamma_\downarrow$ (Fig. 4a). A notable consequence is that for $N = 10^4$, the preparation fidelity for the excited state is higher than the ground state (Fig. 3a, inset).

The time-evolving transition rates (Fig. 4a) are obtained from the stroboscopic quantum-jump traces (Fig. 2d) by using $\Gamma_\uparrow = -\ln(P_{|g\rangle,|g\rangle})/t_{rep}$ and $\Gamma_\downarrow = -\ln(P_{|e\rangle,|e\rangle})/t_{rep}$, where P is the probability to measure the same qubit state in successive measurements and t_{rep} is the repetition time (Supplementary Section F). These rates define the relaxation rate

$\Gamma_1 = \Gamma_\uparrow + \Gamma_\downarrow$ and the equilibrium population of the qubit $p_{eq} = \Gamma_\uparrow/\Gamma_1$. Note that the noise magnitude varies with the qubit population (Fig. 4a), because the rates $\Gamma_{\uparrow,\downarrow}$ are based on conditional probabilities. Remarkably, after a heating sequence with $N = 10^4$, Γ_1 of the qubit is comparably constant (Fig. 4b); in contrast, p_{eq} follows a non-exponential relaxation for timescales up to 50 ms. At the end of the polarization sequence, for the TLSs, we can ascribe a hyperpolarization $p_{eq}^{TLSs} = 97\%$, which—when taking into account the intrinsic loss of the qubit—gives the measured $p_{eq} = 78\%$ (Fig. 4c). Conversely, after a cooling sequence with $N = 10^4$, we extract $p_{eq} = 3.0\%$, as can be ascertained in Fig. 3b using the qubit population $p_q = 2.0\% \approx p_{eq}$ after $1/\Gamma_1$. Hence, the Szilard engine cooled the environment to an effective temperature of 16 mK, which is well below the temperature of the dilution refrigerator (~25 mK) and the effective temperature $T_{eff} = 28.3$ mK corresponding to the idle qubit population $p_{th} = 12.0\%$ (Fig. 2d). The TLS hyperpolarization is even lower, $p_{eq}^{TLSs} = 3.4\% \triangleq 9.9$ mK, limited by the qubit preparation infidelity. The values are extrapolated from the theoretical model, which will be explained in the next paragraph. For both heating and cooling, the hyperpolarization values are among the highest reported in the literature[32,33].

The constant relaxation rate Γ_1 as well as the observed population inversion indicate an environment consisting of TLSs. We, therefore, model the system assuming the qubit to be coupled to a countable number of TLSs with populations p_t^k. The cross-relaxation rates Γ_{qt}^k between the qubit and TLSs are given by[6,34]

$$\Gamma_{qt}^k = \frac{2g^2 \Gamma_2}{\Gamma_2^2 + \delta_k^2}, \tag{1}$$

where δ_k is the detuning between the qubit and kth TLS, g is their transverse coupling strength and Γ_2 is the sum of their decoherence rates. Since the TLSs can, in turn, excite the qubit, we conclude that the qubit and TLSs are close in frequency so that they approximately relax to the same thermal population p_{th} (note that the qubit is well thermalized, as discussed earlier). Finally, we introduce intrinsic relaxation rates for the qubit and TLSs, namely, Γ_q and Γ_t^k, respectively, capturing the remaining environment (Fig. 1b). The dynamics is governed by the so-called Solomon equations[34], extensively used in the field of nuclear hyperpolarization[35]. The rate equations read as follows:
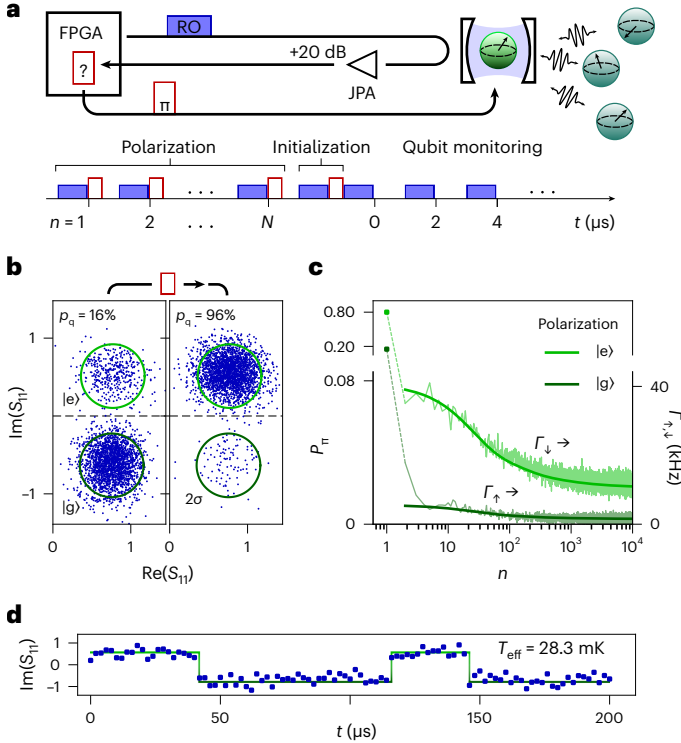
Fig. 2 | Szilard engine in action. a, Schematic of the experiment and control sequence for implementing a Szilard engine. The qubit consists of a fluxonium biased at half-flux (Supplementary Section C) operating at its fundamental transition f_{01} = 1.2 GHz separated by 6.6 GHz from the higher levels. The qubit is coupled to an unknown mesoscopic environment (as shown in Figs. 3 and 4), which can be modelled as an ensemble of TLSs. We start the experiment with the TLS polarization sequence (Fig. 1c) by stabilizing the qubit to either $|g\rangle$ or $|e\rangle$ using N active feedback preparations. This is followed by a qubit initialization in $|g\rangle$ or $|e\rangle$; immediately thereafter, we begin to stroboscopically monitor the qubit state. For polarization and qubit monitoring, the repetition time is t_{rep} = 2 μs, much shorter than the qubit relaxation time $T_1 \approx 20$ μs. Before each of the 2,500 repetitions, we wait for 50 ms to allow the environment to relax. The protocol is orchestrated by the field-programmable gate array (FPGA) controller from Quantum Machines, with an internal real-time feedback latency of ~200 ns (Supplementary Section D provides a schematic of the detailed setup). **b**, Scatter plot of the complex reflection coefficient S_{11} of the readout signal for the qubit in equilibrium (left) and after $|e\rangle$-state preparation (right). The readout integration time is 128 ns, resulting in a separation of 5.6σ (green circles indicate 2σ). **c**, Probability P_π to reset the qubit to its target state during polarization (P_π is corrected for state preparation and measurement errors; Supplementary Section E). Using t_{rep}, the values of P_π can be mapped to the qubit transition rates $\Gamma_\uparrow$ and $\Gamma_\downarrow$ for polarization to $|g\rangle$ and $|e\rangle$, respectively (right-hand axis). The evolution of the rates is captured by the theoretical model derived in the main text (solid lines). **d**, Typical quantum-jump trace during qubit monitoring (as shown in **a**). The solid line indicates the assigned qubit state. JPA, Josephson Parametric Amplifier; RO, readout.

$$\dot{p}_q = -\Gamma_q(p_q - p_{th}) - \sum_k \Gamma_{qt}^k(p_q - p_t^k), \qquad (2)$$

$$\dot{p}_t^k = -\Gamma_t^k(p_t^k - p_{th}) - \Gamma_{qt}^k(p_t^k - p_q), \qquad (3)$$

where we identify the constant qubit relaxation rate as $\Gamma_1 = \Gamma_q + \sum_k \Gamma_{qt}^k$ and the time-dependent $p_{eq} = \left(\Gamma_q p_{th} + \sum_k \Gamma_{qt}^k p_t^k\right)/\Gamma_1$. As a consequence of equation (3), during the polarization time $N \times t_{rep}$, when we enforce $p_q = 0$ or 1, there is an exponential population transfer

between the qubit and each TLS; at the end of the sequence, we expect to find the TLSs polarized (Fig. 2c).

So far, the model in equations (2) and (3) requires two rates for each TLS. To extract meaningful information from the measurements by virtue of equation (1), we need to make simplifying assumptions and reduce the number of fitting parameters. Since we observe the TLS polarization in different qubits and at different qubit frequencies (Supplementary Section I), we expect the TLSs to be randomly distributed in frequency. We simplify this distribution by modelling them to be equally spaced in frequency with $\delta_k = k\Delta + \Delta_0$, where $\Delta_0 \in [0, \Delta/2]$ defines a shift in the TLS ladder with respect to the qubit frequency. This is justified by the fact that we are mainly interested in capturing the slow, non-exponential relaxation at millisecond timescales. With the same argument for all TLSs, we assume the same g and Γ_2. The price we pay for using these simplifications is that the model less accurately captures the initial features of the decay curves, at $t < 300$ μs. Indeed, these features are a fingerprint of the exact configuration of the TLSs; as expected, they fluctuate in time[36,37] (Supplementary Section A).

The simplified model allows to rewrite equation (1) in the compact form $\Gamma_{qt}^k = ab^2/[b^2 + (k + bc)^2]$, showing that g, Δ, Δ_0 and Γ_2 do not independently appear in the model. Instead, $g = \sqrt{a\Gamma_2/2}$, $\Delta = \Gamma_2/b$ and $\Delta_0 = c\Gamma_2$ can be determined for a given decoherence rate from a successful fit of the model. The fit procedure is further restricted by inserting the measured qubit relaxation rate as $\Gamma_1 = 1/21.5$ μs (Fig. 4b), leaving us with only two essential fit parameters, namely, Γ_q and b (Supplementary Section J). The robustness of the model is illustrated by the fact that a fit of only the first millisecond to one of the stronger polarized relaxation curves (for example, polarization to $|e\rangle$ for $N = 10^3$ with initialization to $|g\rangle$ or $|e\rangle$) is sufficient to describe the highly non-exponential relaxation of all the measurements on the entire relaxation range up to 50 ms (Figs. 3 and 4, continuous lines). Details of the fitting procedure are presented in Supplementary Section J.

Using the lower bound of $\Gamma_2 \geq \Gamma_2^q \approx 0.5$ MHz, where Γ_2^q is the decoherence rate of the qubit (Supplementary Section K), we extract $g \geq 2\pi \times 12$ kHz and $\Delta \geq 2\pi \times 167$ kHz. The comparably small coupling strength $g \ll \Gamma_2^q$ is consistent with the fact that we do not observe avoided level crossings in the qubit spectrum. In particular, this argument remains valid even for higher decoherence because g and Δ scale with $\sqrt{\Gamma_2}$ and Γ_2, respectively. Using an upper bound for the decoherence as $\Gamma_2 \approx 1/10$ ns $\ll f_q$, comparable with values reported in another work[20], gives $g < 2\pi \times 170$ kHz and $\Delta < 2\pi \times 35$ MHz.

Furthermore, we can calculate the two contributions of the qubit relaxation: one rate is due to interactions with the TLSs, that is, $\Gamma_{qt}^{TLS} = \sum_k \Gamma_{qt}^k = 35.9$ kHz, and the other is the remaining intrinsic relaxation $\Gamma_q = 10.7$ kHz. We, therefore, identify the TLS bath as the dominant loss mechanism. Remarkably, the fit also indicates that the intrinsic relaxation time exceeds $1/\Gamma_t \geq 50$ ms, which is orders of magnitude longer than previously measured relaxation rates of dielectric TLSs[38–40]. This fact leads us to believe that we are reporting a new type of TLS environment, possibly related to spins[41,42] or trapped quasiparticle TLSs[13]. Finally, we would like to mention that $\Gamma_{qt}^k \geq \Gamma_t$ for $|k| \leq 15$, which means that the qubit is the main decay channel for at least the first few tens of the most resonant TLSs.

Following Szilard's seminal paper[21], the homonymous engine uses measured information as fuel (Supplementary Section L). In the first iteration of a cooling sequence starting from thermal equilibrium at $T = 28.3$ mK, the engine extracts, on average, the internal energy $\Delta U = 0.24 k_B T$ from the qubit, corresponding to an entropy reduction of $0.37 k_B$, which should be compared with the entropy produced by the measurement apparatus ($k_B \ln 2 \approx 0.69 k_B$). From the rate equation, we can calculate the optimal working regime for our Szilard engine. Using the fitted parameters, we infer that the maximum
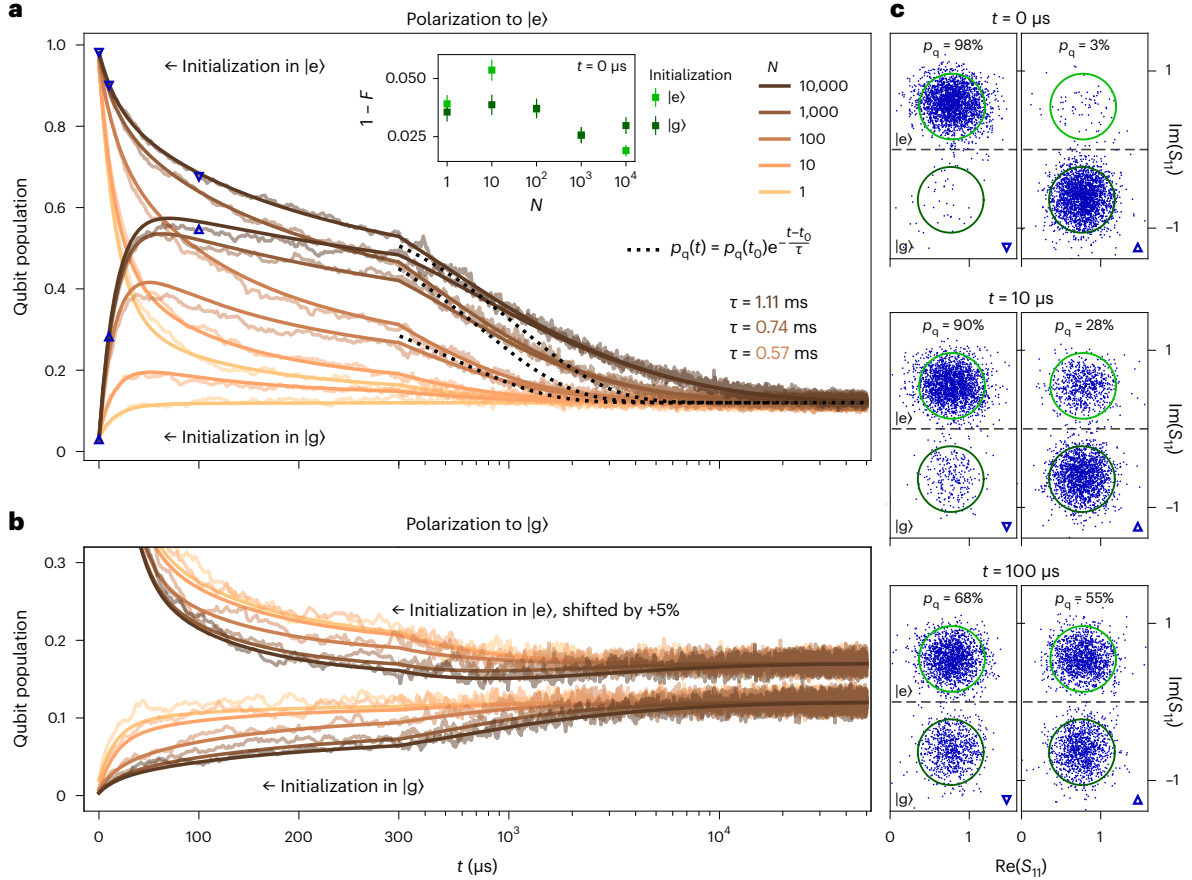
Fig. 3 | Qubit evolution after running the Szilard engine. a, Measured relaxation of the qubit after polarization to $|e\rangle$ for various times $N \times t_{rep}$ followed by initialization in either $|g\rangle$ or $|e\rangle$. Note the logarithmic x axis from 300 µs onwards, which is required to depict the slow relaxation dynamics. The exponential decay curves (dotted lines), with the decay times indicated by the corresponding labels, are guides to the eye to illustrate the non-exponential relaxation of the environment (Supplementary Section G). The inset shows the preparation infidelity of the initialization. We observe an increasing fidelity with N, particularly for the initialization in $|e\rangle$. The error bars show the 1σ confidence intervals of the binomial distribution with 2,500 repetitions. **b**, Measured relaxation of the qubit after polarization to $|g\rangle$ followed by an initialization in either $|g\rangle$ or $|e\rangle$. Compared with **a**, the opposite effect is visible: the environment is cooled by the polarization sequence, demonstrating that the heat flow in the environment is not the trivial result of heating due to repeated microwave readout and control pulses. The top curves are shifted upwards by 5% for better visibility. The continuous lines in **a** and **b** correspond to the theoretical model of equations (2) and (3), simultaneously applied to all the measured curves. **c**, Scatter plots of the complex reflection coefficient S_{11} for the relaxation curves shown in **a** for $N = 10^4$. The left panels illustrate the reduced relaxation of the excited-state population versus time. The right panels demonstrate that the qubit undergoes a population inversion due to interactions with the environment. In particular, the $|f\rangle$ state is not populated, as illustrated by the absence of a third cloud in the S_{11} distribution (Supplementary Section H).

heat reduction of $\Delta Q = 0.11 k_B T$ in the reservoir occurs 68 µs after qubit initialization. Thus, at most half of the extracted heat from the qubit can be used to cool the reservoir. With a similar timescale of $t_{rep} = 100$ µs (Supplementary Section M), we show that the reservoir can also be heated by a sequence of π pulses. However, this procedure, introduced in another work[9], cannot result in population inversion in the reservoir.

In summary, using a superconducting qubit and active feedback, we demonstrated a quantum Szilard engine that can polarize a TLS environment of unknown origin. As a result, the qubit population exhibits remarkably long and non-exponential dynamics due to the intrinsically long decay time of the TLSs, exceeding 50 ms. This showcases the challenges and pitfalls of extracting T_1 from the relaxation data of the qubit population. In our device, we extract T_1 from quantum jumps and show that it is unaffected by the continuous operation of the qubit, ruling out enhanced quasiparticle diffusion[9]. Although T_1 is independent of the environment population, the transition rates $\Gamma_{\uparrow,\downarrow}$ are not. Our results are particularly relevant in the context of quantum processors, where the heating and cooling of the environment is a byproduct of continuous operation. The Szilard engine could be used to study out-of-equilibrium processes or to preferentially reduce one of the qubit transition rates. For example, reducing $\Gamma_\uparrow$ would be beneficial for bosonic codes[43,44].

In our system, quantum coherence between the qubit and TLSs can be neglected, allowing a simple description using the Solomon equations. As quantum hardware continues to improve, coherent interactions and non-Markovian qubit dynamics will start to play a role, raising the bar for quantum error correction strategies. The quantum Szilard engine presented here offers the first glimpse of the challenges facing future hardware, in which coherence improvements also translate into increasingly complex interactions with the environment.
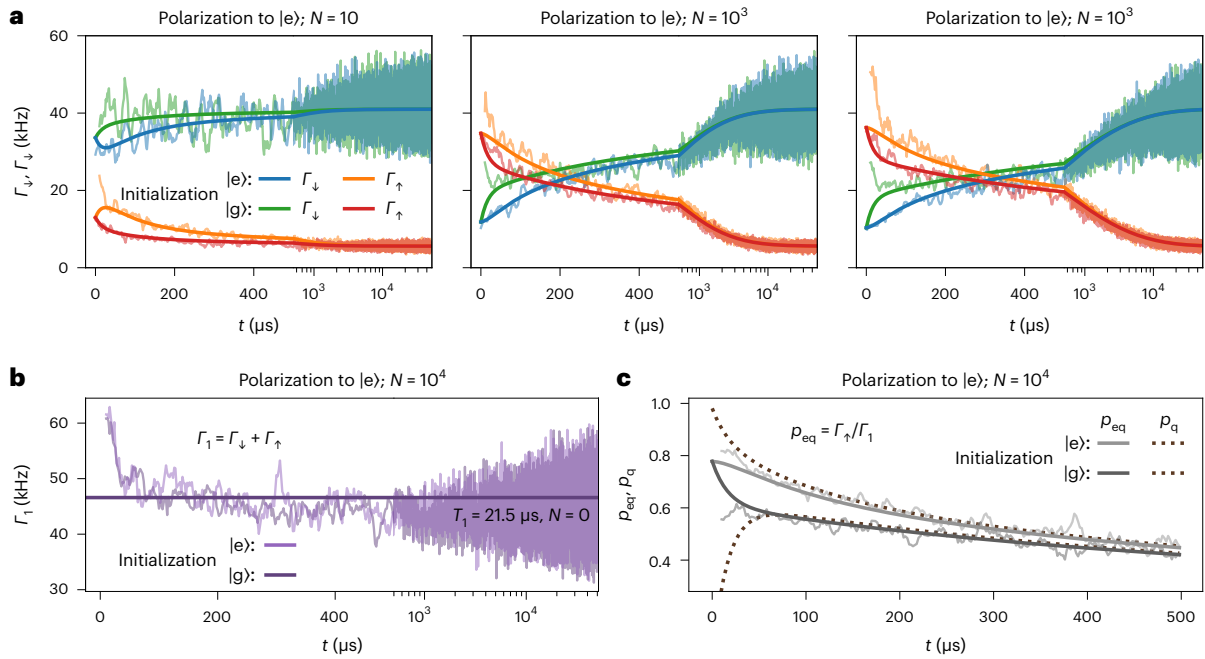
Fig. 4 | Measured population inversion and constant relaxation rate − signatures of the TLS environment. a, Measured (light colour) and calculated (dark colour) qubit transitions rates $\Gamma_{\uparrow,\downarrow}$ following initialization in $|g\rangle$ or $|e\rangle$ and for increasing polarization to $|e\rangle$ from $N = 10$ to 10^3 and 10^4 (left, middle and right panels, respectively). The measured rates are extracted from the same quantum-jump traces used to extract the qubit relaxation (Fig. 3a), with the logarithmic time axis starting at 500 μs. For long polarization times, the rates are reversed in the beginning, meaning that the qubit sees a negative-temperature environment. Note that in all the cases, the $|g\rangle$-state initialization visibly cools the environment, suggesting a heat capacity of only a few energy quanta. To reduce the statistical noise, a five-point moving-average filter was applied corresponding to a 10 μs

window. Furthermore, the first 10 μs of the orange and green curves are omitted due to low statistics; it is unlikely to have two consecutive intervals of $\lesssim 5$ μs between jumps. Similarly, these rates are overestimated in the beginning by preferably detecting short T_1 fluctuations of the qubit. **b**, Relaxation time Γ_1 obtained from the $\Gamma_{\uparrow,\downarrow}$ rates in **a** for $N = 10^4$. The Γ_1 rate is constant compared with the changes in $\Gamma_\uparrow$ and $\Gamma_\downarrow$ (shown in **a**), that is, Γ_1 is independent of the environmental populations, which indicates a TLS environment. **c**, Equilibrium population of the qubit p_{eq} extracted from the $\Gamma_{\uparrow,\downarrow}$ rates. The dashed lines show the corresponding qubit population p_q relaxation taken from Fig. 3a. We extrapolate an effective population of the environment $p_{eq} = 78\%$ at $t = 0$. In all panels, the theoretical curves use the same parameters as that in Fig. 3.

References

1. Ofek, N. et al. Extending the lifetime of a quantum bit with error correction in superconducting circuits. *Nature* **536**, 441–445 (2016).
2. Vuillot, C., Asasi, H., Wang, Y., Pryadko, L. P. & Terhal, B. M. Quantum error correction with the toric Gottesman-Kitaev-Preskill code. *Phys. Rev. A* **99**, 032344 (2019).
3. Google Quantum AI. Exponential suppression of bit or phase errors with cyclic error correction. *Nature* **595**, 383–387 (2021).
4. Cai, W., Ma, Y., Wang, W., Zou, C.-L. & Sun, L. Bosonic quantum error correction codes in superconducting quantum circuits. *Fundam. Res.* **1**, 50–67 (2021).
5. Grabovskij, G. J., Peichl, T., Lisenfeld, J., Weiss, G. & Ustinov, A. V. Strain tuning of individual atomic tunneling systems detected by a superconducting qubit. *Science* **338**, 232–234 (2012).
6. Barends, R. et al. Coherent Josephson qubit suitable for scalable quantum integrated circuits. *Phys. Rev. Lett.* **111**, 080502 (2013).
7. Risté, D. et al. Millisecond charge-parity fluctuations and induced decoherence in a superconducting transmon qubit. *Nat. Commun.* **4**, 1913 (2013).
8. Pop, I. M. et al. Coherent suppression of electromagnetic dissipation due to superconducting quasiparticles. *Nature* **508**, 369–372 (2014).
9. Gustavsson, S. et al. Suppressing relaxation in superconducting qubits by quasiparticle pumping. *Science* **354**, 1573–1577 (2016).
10. Grünhaupt, L. et al. Loss mechanisms and quasiparticle dynamics in superconducting microwave resonators made of thin-film granular aluminum. *Phys. Rev. Lett.* **121**, 117001 (2018).
11. Serniak, K. et al. Hot nonequilibrium quasiparticles in transmon qubits. *Phys. Rev. Lett.* **121**, 157701 (2018).
12. Chu, Y. et al. Creation and control of multi-phonon Fock states in a bulk acoustic-wave resonator. *Nature* **563**, 666–670 (2018).
13. De Graaf, S. E. et al. Two-level systems in superconducting quantum devices due to trapped quasiparticles. *Sci. Adv.* **6**, eabc5055 (2020).
14. Wilen, C. D. et al. Correlated charge noise and relaxation errors in superconducting qubits. *Nature* **594**, 369–373 (2021).
15. Glazman, L. & Catelani, G. Bogoliubov quasiparticles in superconducting qubits. *SciPost Phys. Lect. Notes* 31 (2021).
16. Siddiqi, I. Engineering high-coherence superconducting qubits. *Nat. Rev. Mater.* **6**, 875–891 (2021).
17. Kirsh, N., Svetitsky, E., Burin, A. L., Schechter, M. & Katz, N. Revealing the nonlinear response of a tunneling two-level system ensemble using coupled modes. *Phys. Rev. Mater.* **1**, 012601 (2017).
18. Andersson, G. et al. Acoustic spectral hole-burning in a two-level system ensemble. *npj Quantum Inf.* **7**, 15 (2021).
19. Wang, Z. L. et al. Quantum state characterization of a fast tunable superconducting resonator. *Appl. Phys. Lett.* **102**, 163503 (2013).
20. Lisenfeld, J. et al. Electric field spectroscopy of material defects in transmon qubits. *npj Quantum Inf.* **5**, 105 (2019).

21. Szilard, L. Über die Entropieverminderung in einem thermodynamischen System bei Eingriffen intelligenter Wesen. *Z. Phys.* **53**, 840–856 (1929).

22. Toyabe, S., Sagawa, T., Ueda, M., Muneyuki, E. & Sano, M. Experimental demonstration of information-to-energy conversion and validation of the generalized Jarzynski equality. *Nat. Phys.* **6**, 988–992 (2010).

23. Koski, J. V., Maisi, V. F., Pekola, J. P. & Averin, D. V. Experimental realization of a Szilard engine with a single electron. *Proc. Natl Acad. Sci. USA* **111**, 13786–13789 (2014).

24. Peterson, J. P. S., Sarthour, R. S. & Laflamme, R. Implementation of a quantum engine fuelled by information. Preprint at https://arxiv.org/abs/2006.10136 (2020).

25. Bluhm, H., Foletti, S., Mahalu, D., Umansky, V. & Yacoby, A. Enhancing the coherence of a spin qubit by operating it as a feedback loop that controls its nuclear spin bath. *Phys. Rev. Lett.* **105**, 216803 (2010).

26. Broadway, D. A. et al. Quantum probe hyperpolarisation of molecular nuclear spins. *Nat. Commun.* **9**, 1246 (2018).

27. Córcoles, A. D. et al. Exploiting dynamic quantum circuits in a quantum algorithm with superconducting qubits. *Phys. Rev. Lett.* **127**, 100501 (2021).

28. Gold, A. et al. Entanglement across separate silicon dies in a modular superconducting qubit device. *npj Quantum Inf.* **7**, 142 (2021).

29. Satzinger, K. J. et al. Realizing topologically ordered states on a quantum processor. *Science* **374**, 1237–1241 (2021).

30. Grünhaupt, L. et al. Granular aluminium as a superconducting material for high-impedance quantum circuits. *Nat. Mater.* **18**, 816–819 (2019).

31. Gusenkova, D. et al. Quantum nondemolition dispersive readout of a superconducting artificial atom using large photon numbers. *Phys. Rev. Applied* **15**, 064030 (2021).

32. Yang, A. et al. Simultaneous subsecond hyperpolarization of the nuclear and electron spins of phosphorus in silicon by optical pumping of exciton transitions. *Phys. Rev. Lett.* **102**, 257401 (2009).

33. Wang, H.-J. et al. Sensitive magnetic control of ensemble nuclear spin hyperpolarization in diamond. *Nat. Commun.* **4**, 1940 (2013).

34. Solomon, I. Relaxation processes in a system of two spins. *Phys. Rev.* **99**, 559–565 (1955).

35. Vögeli, B. The nuclear Overhauser effect from a quantitative perspective. *Prog. Nucl. Magn. Reson. Spectrosc.* **78**, 1–46 (2014).

36. Klimov, P. V. et al. Fluctuations of energy-relaxation times in superconducting qubits. *Phys. Rev. Lett.* **121**, 090502 (2018).

37. Thorbeck, T., Eddins, A., Lauer, I., McClure, D. T. & Carroll, M. TLS dynamics in a superconducting qubit due to background ionizing radiation. Preprint at https://arxiv.org/abs/2210.04780 (2022).

38. Neeley, M. et al. Process tomography of quantum memory in a Josephson-phase qubit coupled to a two-level state. *Nat. Phys.* **4**, 523–526 (2008).

39. Lisenfeld, J. et al. Measuring the temperature dependence of individual two-level systems by direct coherent control. *Phys. Rev. Lett.* **105**, 230504 (2010).

40. Lisenfeld, J. et al. Decoherence spectroscopy with individual two-level tunneling defects. *Sci. Rep.* **6**, 23786 (2016).

41. Lee, K. H., Holmberg, G. E. & Crawford, J. H. Optical and ESR studies of hole centers in γ-irradiated Al_2O_3. *Phys. Stat. Sol. A* **39**, 669–674 (1977).

42. Yang, F. et al. Microscopic charging and in-gap states in superconducting granular aluminum. *Phys. Rev. B* **102**, 104502 (2020).

43. Reinhold, P. et al. Error-corrected gates on an encoded qubit. *Nat. Phys.* **16**, 822–826 (2020).

44. Grimm, A. et al. Stabilization and operation of a Kerr-cat qubit. *Nature* **584**, 205–209 (2020).

45. Samkharadze, N. et al. High-kinetic-inductance superconducting nanowire resonators for circuit QED in a magnetic field. *Phys. Rev. Applied* **5**, 044004 (2016).

46. Borisov, K. et al. Superconducting granular aluminum resonators resilient to magnetic fields up to 1 Tesla. *Appl. Phys. Lett.* **117**, 120502 (2020).

47. Quintana, C. M. et al. Observation of classical-quantum crossover of 1/f flux noise and its paramagnetic temperature dependence. *Phys. Rev. Lett.* **118**, 057702 (2017).

48. Reed, M. D. et al. Fast reset and suppressing spontaneous emission of a superconducting qubit. *Appl. Phys. Lett.* **96**, 203110 (2010).

49. von Lüpke, U. et al. Parity measurement in the strong dispersive regime of circuit quantum acoustodynamics. *Nat. Phys.* **18**, 794–799 (2022).

50. Vool, U. et al. Non-Poissonian quantum jumps of a fluxonium qubit due to quasiparticle excitations. *Phys. Rev. Lett.* **113**, 247001 (2014).

51. Nsanzineza, I. & Plourde, B. L. T. Trapping a single vortex and reducing quasiparticles in a superconducting resonator. *Phys. Rev. Lett.* **113**, 117002 (2014).

52. Kumar, P. et al. Origin and reduction of 1/f magnetic flux noise in superconducting devices. *Phys. Rev. Applied* **6**, 041001 (2016).

53. Müller, C., Cole, J. H. & Lisenfeld, J. Towards understanding two-level-systems in amorphous solids: insights from quantum circuits. *Rep. Prog. Phys.* **82**, 124501 (2019).

Author contributions

M.S. and I.M.P. conceived the experiment. N.D. and Y.C. installed and supervised the real-time microwave electronics. M.S. performed the experiment, analysed the data and developed the theoretical model. I.T. and P.W. designed and fabricated the parametric amplifier. R.G. and O.S. provided the real-time microwave electronics for preliminary experiments. P.P. and N.G. carried out additional measurements for the revised manuscript. M.S. and I.M.P. wrote the manuscript. A.S. and I.M.P. supervised the project. All authors discussed the results and contributed to the final manuscript.

Competing interests

The authors declare no competing interests.

Additional information

Correspondence and requests for materials should be addressed to Martin Spiecker or Ioan M. Pop.